Experimental study on rock indentation using infrared thermography and acoustic emission techniques

Qi Liu[1] ⬡, Quansheng Liu[1,3], Yucong Pan[1], Xingxin Peng[2], Penghai Deng[1] and Kai Huang[1]

[1] The Key Laboratory of Safety for Geotechnical and Structural Engineering of Hubei Province, School of Civil Engineering, Wuhan University, Wuhan, Hubei 430072, People's Republic of China
[2] Institute of Rock and Soil Mechanics, Chinese Academy of Sciences, Wuhan, Hubei 430071, People's Republic of China

E-mail: liuqs@whrsm.ac.cn

CrossMark

Abstract

For better understanding of rock fragmentation mechanism and correlative influence factors under the cutter penetration, a set of two-dimensional wedge indentation tests was conducted. Nondestructive detection techniques, including infrared thermography and acoustic emission, were employed to capture rock damage evolution information. Combined with experimental observations, the cavity expansion model (CEM) theory was adopted to interpret the temperature rise differences for different rock damage zones, and the sizes of these zones were quantitatively determined based on the thermal distribution. It was thought that different thermomechanical coupling mechanisms in different damage zones cause their differences in temperature rise degrees. The quantitative estimation for damage zone sizes indicates the plastic zone and core zone initiate and develop sequentially rather than simultaneously. The main influence factors on rock indentation and damage evolution characteristics were also considered, including rock type, wedge indenter geometry and confining stress. Furthermore, some shortcomings of the classical CEM were discussed through the comparison of indentation pressure and damage zone size between the experimental value and theoretical estimation.

Keywords: wedge indentation, damage evolution, infrared thermography, acoustic emission, cavity expansion model

(Some figures may appear in colour only in the online journal)

Nomenclature

a	indenter-rock contact radius	p	indentation pressure
c	rock cohesion	r_1	radius of core zone
d	indenter penetration depth	r_1^*	scaled radius of core zone
d^*	normalized penetration depth	r_2	outer radius of plastic zone
E	elastic modulus of rock	r_2^*	scaled outer radius of plastic zone
F	normal force	ΔT	difference of infrared radiation temperature
h	distance from indenter tip	β	included angle between the wedge indenter surface and rock sample
		ν	Poisson's ratio of rock
		v_p	P-wave velocity of rock

[3] Author to whom any correspondence should be addressed.

ξ_*	normalized radius of the elasto-plastic interface
ρ	rock density
σ_0	lateral confining stress
σ_c	uniaxial compression strength of rock
σ_t	tensile strength of rock
φ	friction angle of rock
ψ	dilatancy angle of rock

1. Introduction

In tunnel construction and other underground openings, rock mechanical response characteristics under cutter interaction have a great effect on the work efficiency of tunnel boring machine (TBM). With the extensive utilization of TBM in mining, transportation and hydropower industries, frequent cutter changing induced by cutter consumption during the rock excavation has become an outstanding challenge for engineers (Dahl *et al* 2007, Hassanpour *et al* 2014). A proper understanding of rock fragmentation mechanism by cutters and correlative influence factors is the foundation of efficient cutters selection, design, arrangement and optimized TBM operation mode, however, it still remains elusive (Cook *et al* 1984, Chen and Labuz 2006, Chen *et al* 2009, Ma *et al* 2011, Entacher *et al* 2015, Li *et al* 2016).

The primary process of rock cutting begins with the development of a crushed zone induced by cutter penetration. Thus, rock cutting by disc cutters or rippers can be generally simplified as the indentation by a wedge or other shaped indenters (Mishnaevsky 1995, Chiaia 2001, Liu *et al* 2002, Chen and Labuz 2006, Innaurato *et al* 2007). Resulting from the practical difficulty to experimentally investigate the entire process of rock fragmentation under the cutter penetration due to the invisibility of damaging and cracking behavior inside the rock, many simplified models were proposed. Hertzian analysis based on elastic contact was first presented to expound the elastic stress field of a flat sample loaded by a relatively hard spherical indenter (Lawn and Wilshaw 1975). Due to the singularity of elastic stress field in the tip point for sharp indenter such as the cone and pyramid, Marsh (1964) and Johnson (1970) proposed a simplified cavity expansion model (CEM) in which the crushed core zone of rock under a blunt indenter can be approximately regarded as the expanding cavity, and plastic damage and inelastic deformation are also considered in other damage zones. This model was further generalized by Alehossein *et al* (2000) and Huang and Detournay (2013). Meanwhile, to analyze the median crack initiation and fracture propagation, Lawn and Evans (1977), Lawn and Marshall (1984) introduced the linear fracture mechanics into the indentation fracture analysis of brittle solids.

Through simplifying the rock cutting process as a two-dimensional indentation test, direct and real-time observations of the rock fragmentation under the cutter penetration were carried out. Chen and Labuz (2006) conducted a set of wedge indentation tests using granite and sandstone combined with the nondestructive detection techniques, including acoustic emission (AE) and electronic speckle pattern interferometry. In the analysis, the AE cluster distribution was used to quantitatively estimate the damage zone size beneath the indenter. Actually, the occurrences of AE events induced by microcracks are partly random in the stressed field due to the discrete distribution of natural defects inside the rock (Zietlow and Labuz 1998). Meanwhile, location deviations of AE events near the indenter will increase with continuous accumulation of rock damage because the latter can intensify the heterogeneity of velocity field in the rock. Therefore, quantitative and accurate evaluation of the damage zone size based on located AE events may require further verification. Zhang *et al* (2012) and Song *et al* (2013) investigated the onset of fracture and the crack length evolution of a plate sandstone sample penetrated by a cylinder with the application of the optical monitoring technique, digital image correlation. It was revealed that the splitting fracture mechanism play the dominant role in the failure process of sandstones under indentation. Yadav *et al* (2015) studied the effect of indentation parameters on rock deformation field and accompanying volume change through the plane strain wedge indentation tests of a model porous brittle solid. Particle image velocimetry analysis of high-speed and high-resolution images of the indentation region was also conducted. However, it is thought to be difficult to effactually obtain the quantitative insights of brittle rock materials such as granite under indentation using the aforementioned optical or image-based techniques, due to its unapparent deformation before the occurrence of the macroscopic fracture.

While subjected to different stress fields, rock material may deform elastically, elasto-plastically or totally plastically. During the deformation process, part of elastic energy accumulated inside will be transformed into other types, such as wave energy and thermal energy which are respectively caused by the microcracks formation and the thermo-mechanical coupling effect. Meanwhile, the energy consumption and conversion can cause infrared (IR) radiation and thermal variation, based on which the infrared thermography (IRT) was successfully applied in many rock mechanics studies as a promising nondestructive monitoring technique (Minh Phono 1990, Wu *et al* 2000, 2002, Shi *et al* 2007, He 2011, Sun *et al* 2017).

The present investigation aims to experimentally reveal the rock fragmentation mechanism and correlative influence factors under the penetration by wedge indenters, which can be regarded as the simplified models of real V-type disc cutters. Combined with nondestructive detection techniques, IRT and AE, the entire process of rock damage evolution under indentation was effectively observed and quantitatively analyzed. The CEM was adopted to reveal the rock damage mechanism in detail and quantitatively determine the sizes of different damage zones, and the correlative influence factors of rock indentation were also explored by comparative tests. Furthermore, some shortcomings of the classical CEM were discussed through the comparison of indentation pressure and

Table 1. Physical and mechanical parameters of the granite and sandstone.

Parameters	σ_c (MPa)	E (GPa)	ν	σ_t (MPa)	c (MPa)	φ (°)	ν_p (m s^{-1})	ρ (g cm^{-3})
Granite	148.45	37.22	0.26	6.68	26.28	56.68	3343	2.64
Sandstone	60.46	13.55	0.29	2.36	18.64	40.69	2573	2.25

damage zone size between the experimental value and theoretical estimation.

2. Experiment

2.1. Rock samples preparation

To investigate the indentation effect of wedge indenters on different types of natural rocks, granite (a typical igneous rock) and sandstone (a typical sedimentary rock), respectively taken from Henan and Chongqing province, China, were chosen. According to the testing methods suggested by ISRM (Brown 1981), the main physical and mechanical parameters of these two rock types are summarized in table 1 by conducting uniaxial compression tests, Brazilian tests, triaxial compression tests, and sound velocity tests. Wherein, $\sigma_c =$ uniaxial compressive strength, $E =$ elastic modulus, $\nu =$ Poisson's ratio, $\sigma_t =$ tensile strength, $c =$ cohesive strength, $\varphi =$ friction angle, $\nu_p =$ velocity of P-wave and $\rho =$ density.

In order to ensure the similar mechanical properties and avoid the possible size effect, all rock samples were incised from a same large granite or sandstone block, and manufactured in the same dimensions of $190 \times 150 \times 22$ mm (length×height×thickness). Meanwhile, the four edge angles were ground strictly to 90° to ensure that the lateral pressure could be loaded smoothly and evenly on the rock sample sides. Grinding and polishing treatments of the rock sample surfaces are also essential to improve their flatness, which is helpful for a steady initial thermal field. After grinding and polishing, all rock samples were dried at 50 °C for about 24 h.

2.2. Instruments and system configuration

A set of indentation tests was conducted to simulate the rock failure process under the penetration by wedge indenters. The main experimental instruments include a loading and confining system, a thermal infrared imager and a multichannel AE system.

2.2.1. The loading and confining system. A two-dimensional indentation test device was designed and manufactured as shown in figure 1(a). It contained an indentation test frame with sufficient stiffness to provide the needed mechanical reaction, a horizontal hydraulic jack and two bearing plates to exert the lateral confining stress up to 60 MPa on the sides of the above-mentioned rock samples, a series of wedge indenters with different geometric parameters to penetrate rock, and a servo-controlled testing machine to provide the

normal indentation force. To investigate the influence of wedge indenter geometry on rock fragmentation, four indenters with wedge angles of 60°, 90°, 120° and 150° were prepared as shown in figure 1(b). They all had sharp tips and were 40 mm in width and 40 mm in edge length. Meanwhile, three indenters with a same wedge angle of 120° but different wear flat widths including 2 mm, 4 mm, and 6 mm, were also set to imitate the real V-type cutters in site with different wear degrees. These wedge indenters were manufactured using heat-treated alloy steel with high hardness (HRC 64) to ensure they could be approximately considered as rigid bodies during indentation interaction process. The servo-controlled testing machine RMT-301 is developed by the Institute of Rock and Soil Mechanics, Chinese Academy of Sciences. It could automatically record the entire loading process before and after the peak.

2.2.2. The monitoring equipment. To obtain the detailed information of rock fragmentation process under wedge indentation, two nondestructive detection devices, a thermal infrared imager and a multichannel AE system were employed.

One cooled medium-wave thermal infrared imager FLIR SC7700M was employed to detect the thermal field change on the front surfaces of rock samples. Its main technical indices include a minimum detection temperature difference of 20 mK, a graphic resolution of 640×512 pixels and a maximum scanning rate of 115 Hz. During the test, the imager was arranged 0.85 m away from the rock sample, and the scanning rate was set to 25 Hz.

The PCI-2 AE testing system produced by the Physical Acoustic Corporation (PAC) was simultaneously employed to record the damage evolution process of the rock sample penetrated by a wedge indenter through the 2D AE location. The role of AE monitoring is to crosscheck to observation result of damage evolution process gotten by IRT detection. To provide a good coverage for the monitored zone of the rock sample, six Nano 30 AE sensors with an operating frequency range of 125–750 kHz were attached to the back surface of rock sample as shown in figure 1(c). Vacuum grease was used as the couplant to ensure the good contact between the sensor face and the sample surface for signal detection. During the test, the sampling frequency and threshold level of AE system were set to 2 MHz and 45 dB, respectively.

2.3. Experimental setup and procedure

For the purpose of investigating the main influence factors on the rock fragmentation under indentation, some test variables were set, including (1) two types of rocks with different
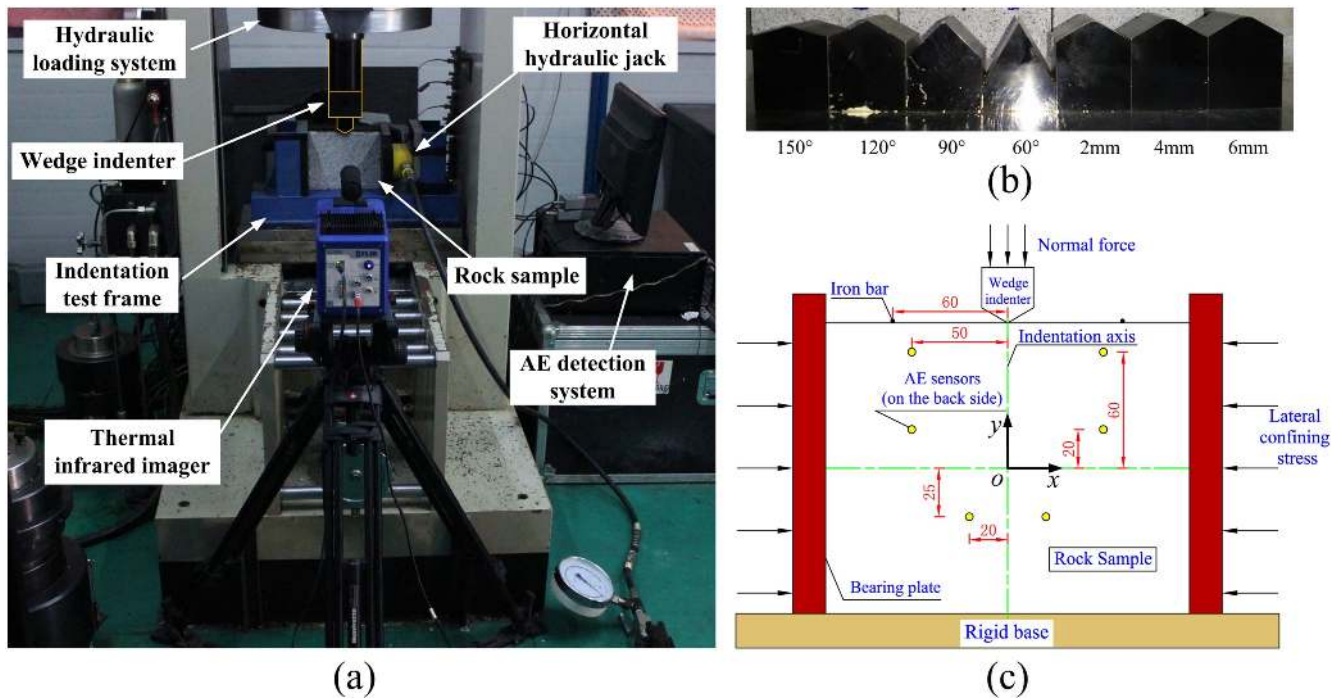
Figure 1. Test system configuration: (a) testing and data acquisition system of indentation, (b) wedge indenters with different geometrical features and (c) sketch of the indentation test (unit: mm).

Table 2. Labels of all rock samples.

Test variables	Variable values and rock sample labels				
Wedge angle/°	60	90	120	150	
	SA60	SA90	S0	SA150	
	GA60	GA90	G0	GA150	
Wear flat width/mm	0	2	4	6	
	S0	SW2	SW4	SW6	
	G0	GW2	GW4	GW6	
Lateral confining stress/MPa	0.1	2	5	8	11
	S0	SC2	SC5	SC8	SC11
	G0	GC2	GC5	GC8	GC11

mechanical properties; (2) wedge indenters with different geometric parameters, i.e., wedge angles of 60°, 90°, 120° and 150° and wear flat widths of 0, 2, 4 and 6 mm; and (3) lateral confinement of 0, 2, 5, 8 and 11 MPa. All rock samples and their labels are listed in table 2.

Here, different symbols in the rock sample labels have different meanings. 'S' denotes the sandstone sample, 'G' denotes the granite sample, 'A' denotes the wedge angle, 'W' denotes the wear flat width, 'C' denotes the confining stress, and the number denotes the value of the corresponding test variable. Specially, 'G0' and 'S0' respectively represent the granite and sandstone samples under the penetration of wedge indenter with a 120° wedge angle, a sharp tip, and a lateral confinement of 0.1 MPa which aims to restrain the free deformation of rock and avoid overly rapid failure after the peak force. They contribute as the comparison with other samples under different loading conditions. Rock samples in

the lateral confinement group were penetrated by the same indenter but with different lateral confining stress. However, rock samples in groups of wedge angle and wear flat width were penetrated using indenters with different geometric parameters but with the same lateral confining stress of 0.1 MPa.

Before beginning the test, two short and small iron bars were pasted on the top face of the rock sample along the indentation symmetry axis, with a constant relative distance of 120 mm. The role of iron bars is to calibrate the real size of thermogram scale. Several iterations of pencil-lead break tests were conducted as suggested by ASTM American Society for Testing and Materials (2015) to ensure good coupling between the AE sensors and rock surfaces and calibrate the 2D AE location accuracy. After the lateral confinement was exerted to the predetermined level slowly and the thermal field of the rock sample surface reached a steady state, the
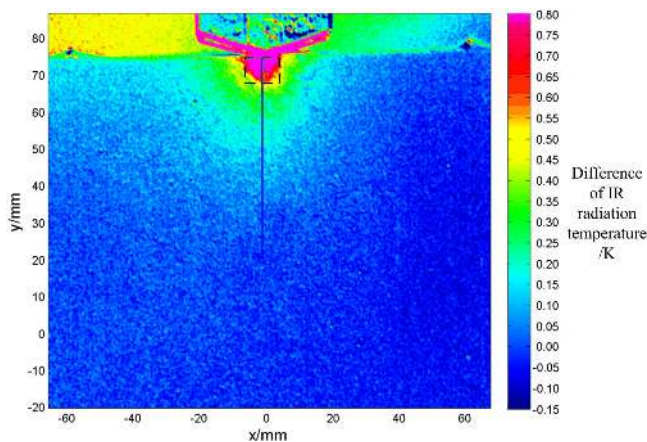
Figure 2. Differential thermogram of the granite under 150° wedge indenter (GA150) before the macroscopic fracture.

normal indentation force began to be imposed at a constant penetration rate of $0.005 \, \text{mm s}^{-1}$ with thermal variation and AE information recorded synchronously and continuously. The indentation would continue for a certain penetration depth after a great force drop and a macroscopic fracture emerged to make the rock failure pattern more obvious. Furthermore, to reduce the environmental interference in the detection of IR thermal radiation emitted from the rock surface, only LED illuminants whose light spectrum does not contain infrared were used in a closed room and personal walking was forbidden during the test. The ambient temperature and environmental humidity in the laboratory were also recorded as $16.7\,°C$ and 66%, respectively.

3. Result analysis

3.1. Damage evolution process

Infrared thermogram can reflect the thermal distribution on the rock sample surface. To highlight its variation and reduce the influence induced by environmental interference and uneven emissivity of the rock sample surface, the differential methodology was used for IR thermograms of rock. It means that the first frame of the thermographic picture at the initiation of indentation loading was used as a benchmark reference for calibration of the temperature changes of the following IR thermograms (He 2011). Figure 2 shows the typical differential thermogram for the granite sample penetrated by 150° wedge indenter before the obvious macrocrack occurs. The following analyses of IR thermogram are all based on the differential results.

Under the penetration of wedge indenter, the phenomenon of discrepant temperature rise occurred on the rock sample surface. There existed a high temperature region beneath the indenter tip, which corresponded to the stress concentration area caused by indentation according to stress distribution analysis of elastic indentation by Truman *et al* (1995, 1996). For the area far from the indenter tip, lower temperature rise appeared. Meanwhile, the thermal field was almost symmetrical about the indentation axis. It can be

concluded that the emergence of high IR radiation temperature is the result of dissipation of accumulated mechanical energy in the rock under indentation. To reveal the rock damage evolution mechanism quantitatively, a rectangular area and a profile along the centerline of the rock sample under the indenter were chosen as research subjects as shown in figure 2, and their thermal distribution and thermal evolution characteristics were analyzed. Specially, the average infrared radiation temperature of the rectangular area was recorded as AIRT.

Figure 3 illustrates the relationship between the indentation force, AIRT, AE hits, and penetration depth. Here, the left *Y*-axis represents the indentation force divided by the thickness of rock sample and two right *Y*-axes are AIRT and AE hits, respectively. Before the cracking point, the indentation force and AIRT increased linearly with the penetration depth. Additionally, AE hits began to undergo a rapid rise at about 50% of peak foce after an initial quiet period. In the stress concentration area of rock sample, partial accumulated mechanical energy was continuously transformed into thermal energy and wave energy with the occurrence of plastic damage and microcracks, which resulted in the increase of AIRT and AE hits. When stress state of the rock sample reached the critical condition, a median macrocrack emerged accompanied by a sudden drop of the indentation force and a dramatic leap of AIRT and AE hits, which reflected the violent energy release and conversion. Due to the lateral confinement, the force curve after the peak did not enter the residual strength state and underwent the repeated rise-drop behavior accompanied by the repeated energy accumulation and release. Meanwhile, every great force drop corresponded to a notable rise of AIRT and AE hits, reflecting the new occurrence of macroscopic fragmentation. To reveal the evolution mechanism of damage zone before the cracking point, A–F points, respectively corresponding to 20%, 40%, 60%, 80%, 100%, and 110% of the penetration depth at the cracking point, are chosen.

The evolution sequence of differential thermograms of GA150 under indentation is illustrated in figure 4. Initially, the IR thermogram (figure 4(A)) shows that a temperature rise area occurred just beneath the indenter tip. The area range progressively expanded and the amplitude of temperature rise gradually grew with the increasing penetration depth (figures 4(B)–(D)). Figure 4(E) is the previous frame of the thermogram just before the macrocrack occurred. From the figure, the high temperature area was approximately semicircular and symmetric about the indentation axis, and the temperature rise of the core exceeded 0.8 K. However, the region far from it exhibited no noticeable thermal variation. The thermogram (figure 4(F)) after the cracking point can reflect the position of the macrocrack well with a significant infrared abnormity strip.

The fragmentation characteristics of rock under the penetration by wedge indenter is consistent with the classical CEM as shown in figure 5. The area below the wedge indenter can be divided into three zones, namely, (1) the semicircular hydrostatic core with radius r_1, in which the stress is in an approximately hydrostatic state and evenly
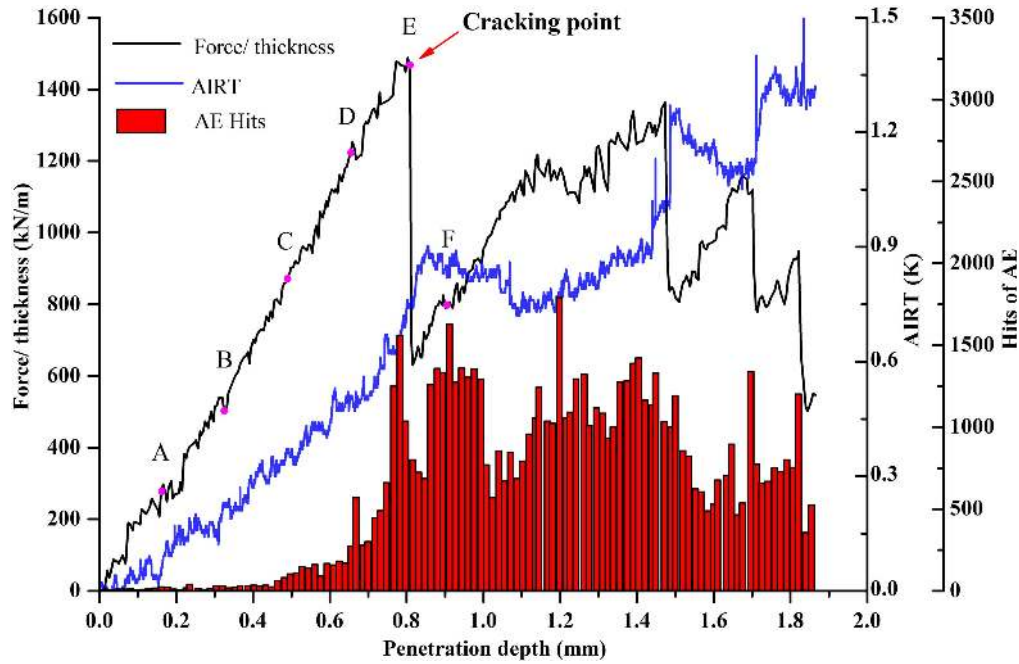
Figure 3. Mechanical response of granite under the 150° wedge indenter with no wear flat.
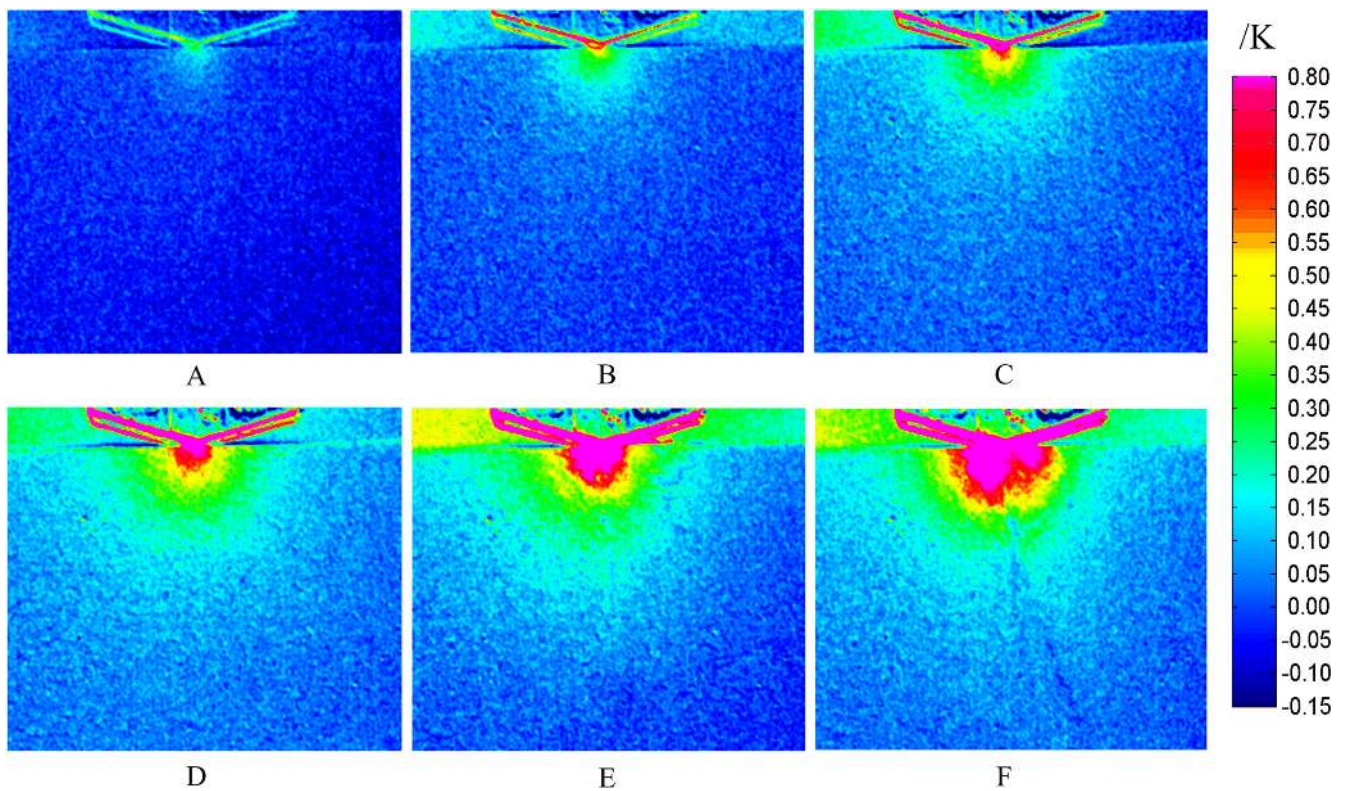

Figure 4. Evolution sequence of differential thermograms of GA150 under indentation.

exerted on its surroundings and rock material tends to shatter when crushed; (2) the plastic zone with an inner radius r_1 and an outer radius r_2, in which the rock is assumed to behave as an elastic-perfectly plastic material obeying the Mohr–Coulomb yield criterion (Alehossein *et al* 2000); (3) the elastic zone, in which reversible deformation is generated without cracking (Chen *et al* 2009, Li *et al* 2016). Combined with

the CEM theory, it is considered that the main mechanisms of the temperature rise in the core zone, plastic zone and elastic zone can be attributed to the thermofracture effect, thermoplastic effect and thermoelastic effect, respectively (Sun and Hsu 1996). Different thermomechanical coupling mechanisms can bring about temperature rises with different degrees as shown in figure 4, which can act as the basis for
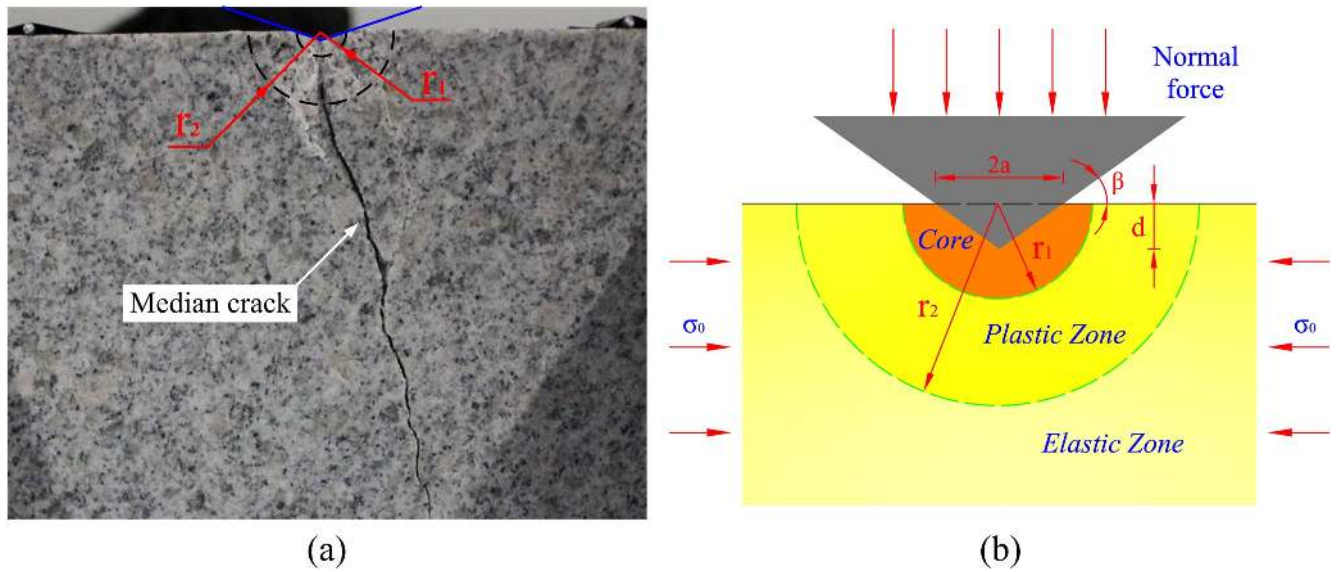
Figure 5. Rock indentation and failure theory: (a) failure pattern of rock sample GA150 and (b) cavity expansion model.
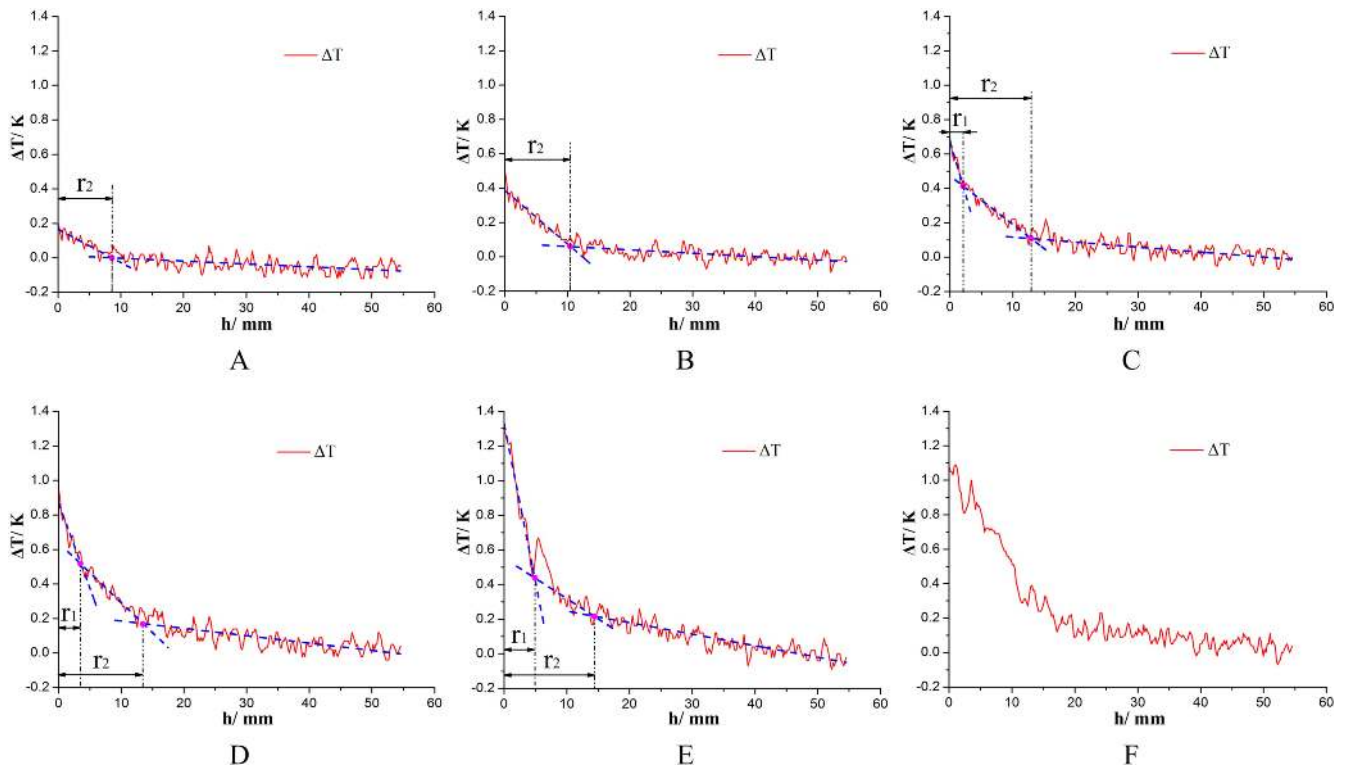

Figure 6. Evolution sequence of thermal distribution along the centerline of the rock sample GA150 and the sizes determination for different damage zones.

the quantitative determination of corresponding damage zone range.

Figure 6 shows the evolution sequence of thermal distribution along the centerline of the rock sample GA150, wherein '*h*' denotes to the distance in the reverse *y*-direction from the indenter tip and 'ΔT' denotes the increment of IR radiation temperature. At different indentation stages, there exists a similar but significant trend that the IR radiation temperature decreases with segmented slopes along the

indentation centerline. Clienti *et al* (2010) and La Rosa *et al* (2014) determined the fatigue limits of materials based on the slope change of thermal variations of spots on specimens including plastics and metals. Combined with the above determination methodology and the CEM theory, the method of piecewise linear fitting was adopted to quantitatively determine the sizes of different damage zones. When the penetration depth was still little (figures 6(A), (B)), the profile could be generally divided into two parts, i.e., the plastic zone
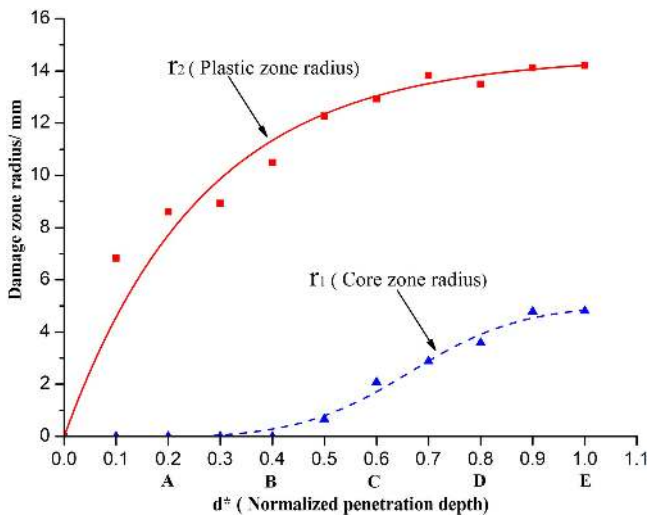
Figure 7. The relationship between the damage zone radius and normalized penetration depth.

with the outer radius r_2 and elastic zone, and the abscissa value of the intersection point of two adjacent fitted lines was used to estimate the radius of the elasto-plastic interface. With the increase of penetration depth, the profile could be fitted with three parts, i.e., the core zone with the radius r_1, plastic zone and elastic zone (figures 6(C), (D)). Specially, it was observed that a remarkable temperature leap occurred near the interface of the core zone and plastic zone just before the median macrocrack emerged (figure 6(E)) and similar phenomenon could be also observed in other samples. It was thought to result from violent microcracking activity there. The relationship between the damage zone radius (r_1 and r_2) and normalized penetration depth (before the cracking point) is shown in figure 7. From the figure, it is clear that the plastic zone radius r_2, rapidly increases before about 0.4 of the normalized penetration depth, and after that it grows slowly and gradually approaches a constant. The r_2 curve approximately accords with the logarithmic trend, and the final value of r_2 at the cracking point is 14.21 mm. In contrast, the core zone does not appear until the expansion of plastic zone begins to slow down. The final radius of core zone is 4.81 mm at the cracking point. The development rule of the rock damage zone under a wedge indenter suggests that the plastic zone and core zone initiate and develop sequentially, which is inconsistent with the theory of the classical CEM. The latter assumes the plastic zone and core zone initiate and develop simultaneously.

To crosscheck the observation of the infrared detection, the evolution sequence of accumulated AE events is depicted as figure 8 in colored scatter diagrams, wherein the point color close to red represents the high event energy and that close to blue represents the low event energy. To improve the location accuracy, only AE events detected by six sensors meantime were shown. Through the pencil-lead break tests, the mean location error of hypocenters in the coverage zone of sensors array was calculated to be within ±3 mm for the intact granite sample using the two-dimensional simplex location algorithm.

AE events caused by microcracks can reflect the development of rock damage. Initially (figures 8(A), (B)), some AE events clustered under the indenter due to stress concentration, which corresponded to the rapid expansion of the plastic zone. With the further increase of penetration depth (figures 8(C), (D)), more AE events were located below the indenter, and a significant localization of AE events was observed in the vicinity of the plastic zone which was determined by IR thermogram. It reflected the further deterioration of rock material in the plastic zone and indicated that the crushed core zone began to develop with the onset of the complete loss of rock mechanical resistance near the indenter tip. When it approached the peak force (figure 8(E)), there existed an explosion of located microcracks, especially AE events with high energy in the plastic zone, which implied the initiation of the critical median macrocrack. Meanwhile, some AE events were also located far from the damage zone during the indentation process. It can be mainly attributed to the discrete mechanical response of rock under the cutter penetration because of the heterogeneity of rock property. On the other hand, the increasing location deviation induced by wave reflection and rock damage accumulation is also a significant reason. Like the IRT observation, the evolution and distribution characteristics of AE events with different energy can reflect the development process of rock damage range and damage degree under the penetration by wedge indenter. However, it seems difficult to accurately determine the sizes of the damage zones including the core zone and the plastic zone, merely according to the located AE events because of their dispersion and increasing deviation in the test. It can be thought the quantitative analysis based on IRT observation is more intuitive and more accurate to reflect the rock damage development than that based on AE detection in the present two-dimensional indentation tests. Therefore, the IRT observation is the main methodology for the following damage analysis of rock under different indentation conditions.

3.2. Influence of wedge angle

To reveal the influence of geometric parameters of indenters on rock damage and fragmentation development, indenters with different wedge angles of 60°–150° were used in indentation tests. Figure 9 shows the typical IR thermograms of samples G0 and SA150, i.e., the granite sample penetrated by a 120° wedge indenter and the sandstone sample penetrated by a 150° wedge indenter. Similar temperature rise characteristics can be observed, namely there exists greater temperature rise in the area close to the indenter tip than that far from it. As macrocracks of different rock samples occurred at different critical penetration depths, scaled damage zone radii r_1^* and r_2^* (r_1 and r_2 at the cracking point divided by the corresponding critical penetration depths) were defined to evaluate the damage effect of different indenters. The scaled damage zone radius can reveal the damage efficiency of an indenter with unit penetration depth to some extent. The relationships between the scaled damage zone radii and wedge angles are illustrated in figure 10. These scatters can be well fitted using quadratic curves, and the peak values of the
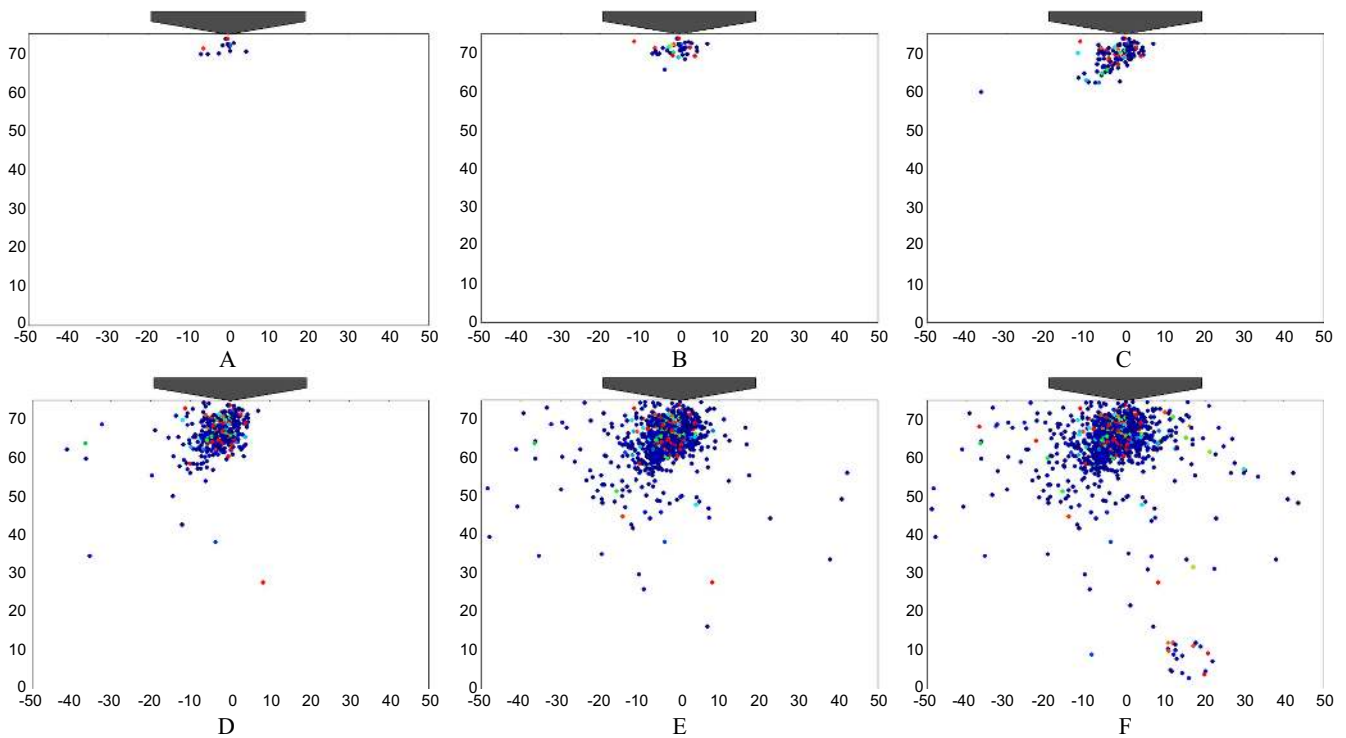
Figure 8. Evolution sequence of the accumulated AE events of GA150 under indentation. (The point color close to red represents the high event energy and that close to blue represents the low event energy.)
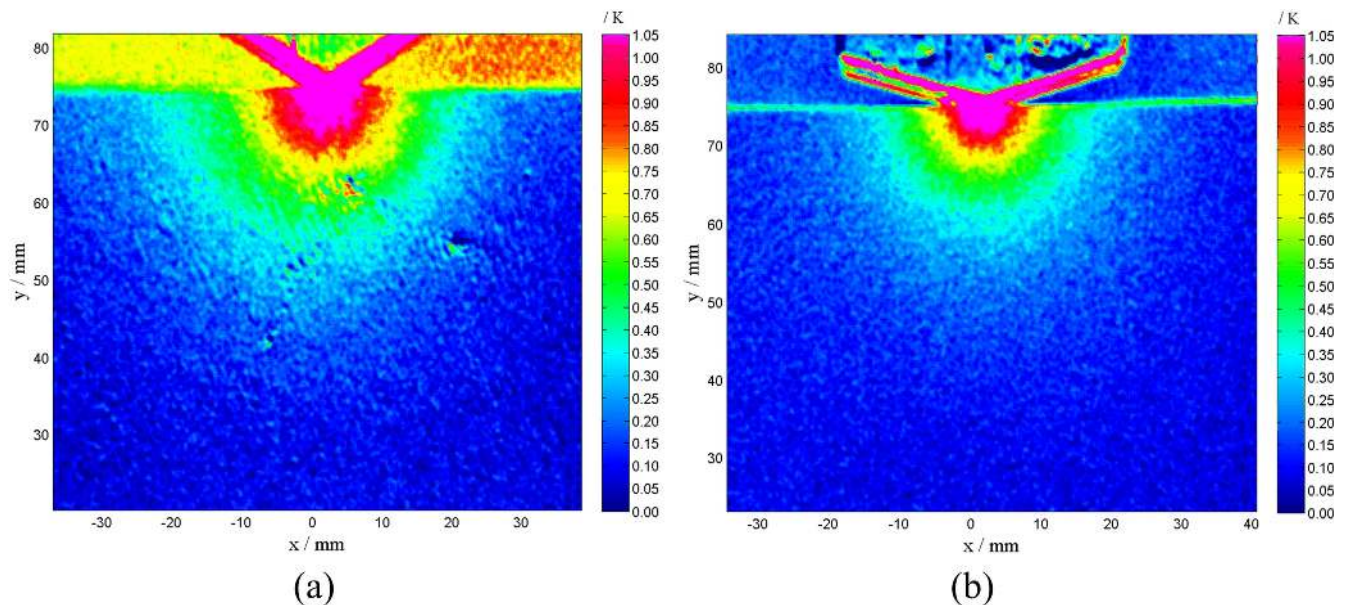

Figure 9. Thermograms of rock samples penetrated by indenters with specific wedge angles, (a) G0 and (b) SA150.

two scaled damage zone radii r_1^* and r_2^* both approximately appear at a wedge angle of 120°. Moreover, the influence of wedge angle on rock damage efficiency is more significant for sandstone than that for granite. Because efficient rock fragmentation mainly results from the rock chips formed between two adjacent cutters, wider damage zone contributes to the efficient rock breakage. It is inferred that the V-type disc cutter with a wedge angle of 120° may have greater working efficiency when cutting rock, especially for rocks with medium strength like sandstone.

3.3. Influence of wear flat width

V-type disc cutters are usually mounted in combination with the constant cross section (CCS) disc cutters or chisel cutters for TBM excavation in complex geologies due to their
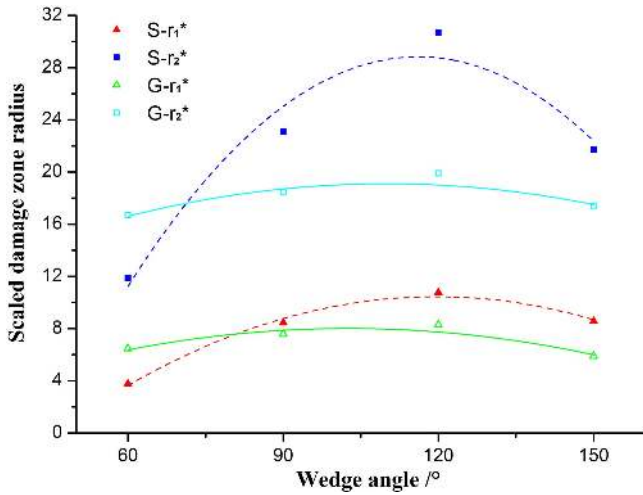
Figure 10. Relationship between the scaled damage zone radii and wedge angles.

efficient performance in rock cutting (Guclucan *et al* 2009, Bilgin *et al* 2012). However, the progressive change of cutter-rock contact area caused by uneven wear of cutter tips usually results in the rapid reduction of cutting efficiency of V-type cutters when excavating in hard and abrasive rock strata (Balci and Tumac 2012). To simulate real cutters in site with different wear degrees, indenters with varying wear flat widths in the range of 0–6 mm were applied in the indentation tests.

After r_1 and r_2 are determined based on the thermal distribution along the centerline of the rock sample, the outlines of core and plastic zones are plotted along isothermal curves in thermogram (figure 11). Under the penetration by a wedge indenter with a specific wear flat, the form of rock damage zone is no longer coincident with the semicircular shape of the classical CEM but instead shows the semiellipse shape, which means the scale of the damage zone in the axial direction is larger than that in the transverse direction. The relationship between the nominal scaled damage zone radii (r_1^* and r_2^*) and wear flat width is shown in figure 12. The nominal r_1^* and r_2^* increase approximately linearly with the development of the penetration depth. It indicates that more indentation work is consumed for the formation of damage zone in the axial direction than that in the transverse direction, which is unfavorable for efficient formation of rock chips between two adjacent cutters. Meanwhile, the force-penetration curve exhibits greater peak force and brittle force drop with the increase of wear flat width (shown in figure 13) when compared with that in the figure 3. Brittle rock fragmentation and greater load drop may cause greater thrust, more violent cutterhead vibration and more serious cutter consumption for TBM. The cutter-rock contact area will progressively increase with the wear development of V-type cutter tips, therefore disc cutters with V-type cross sections are generally replaced by CCS disc cutters in the field of TBM excavation except in some special cases like hard rock or non-abrasive stratum to reduce the required thrust for TBM cutterhead (Balci and Tumac 2012).

3.4. Influence of confining stress

In the deep rock excavation using TBM, high geostress is often confronted. The confining stress is considered as shown in table 2 in the present tests to investigate its influence on rock fragmentation under the cutter penetration.

It is found that for two different rock types, when the lateral confining stress is less than a critical value the brittle failure pattern occurs with a macrocrack running parallel to the indentation axis or skewed from it and when the lateral confining stress exceeds it the ductile failure pattern occurs with the spalling failure of rock under indentation. It accords with the observation of rock failure depicted by Zhang *et al* (2012). In the present tests, the critical confining stress is found to be approximately equal to the tensile strength of rock. Furthermore, an interesting phenomenon was observed that when rock sample failed in brittle failure pattern, the cracking angle of the inclined macrocrack (shown in figure 14) increased with the lateral confining stress (shown in figure 15), which accords with the conclusions of the numerical simulation by Huang *et al* (1998) and the three-dimensional indentation test by Yin *et al* (2014). Although the experimental phenomenon may be insufficient to reflect the influence of confining stress on real rock fragmentation under the cutter penetration because the front and back sides of rock samples are free of stress confinement in the present two-dimensional indentation tests, the trend of brittle-ductile transition of the rock failure pattern with the increase of confining stress is still consistent with that concluded by the three-dimensional indentation tests of Yin *et al* (2014).

4. Discussion

4.1. Comparison between experiment and theory

According to the CEM based on the Mohr–Coulomb yield criterion, the theoretical estimation of the indentation pressure and damage zone size can be calculated using the following equations (1)–(6) for geometrically self-similar blunt wedge indenters (Huang *et al* 1998, Alehossein *et al* 2000, Chen and Labuz 2006).

$$(1 + \mu)\xi_*^{(K_d+1)/K_d} - \mu\xi_*^{(K_p-1)/K_p} = \gamma, \quad (1)$$

$$\gamma = \frac{2(K_p + 1)G\tan\beta}{\pi\sigma_c}, \quad (2)$$

$$K_p = \frac{1 + \sin\varphi}{1 - \sin\varphi} \text{ and } K_d = \frac{1 + \sin\psi}{1 - \sin\psi}, \quad (3)$$

$$\mu = \frac{\lambda K_p}{K_p + K_d}, \quad (4)$$

$$\lambda = \frac{(K_p - 1)(K_d - 1) + (1 - 2\nu)(K_p + 1)(K_d + 1)}{2K_p}, \quad (5)$$

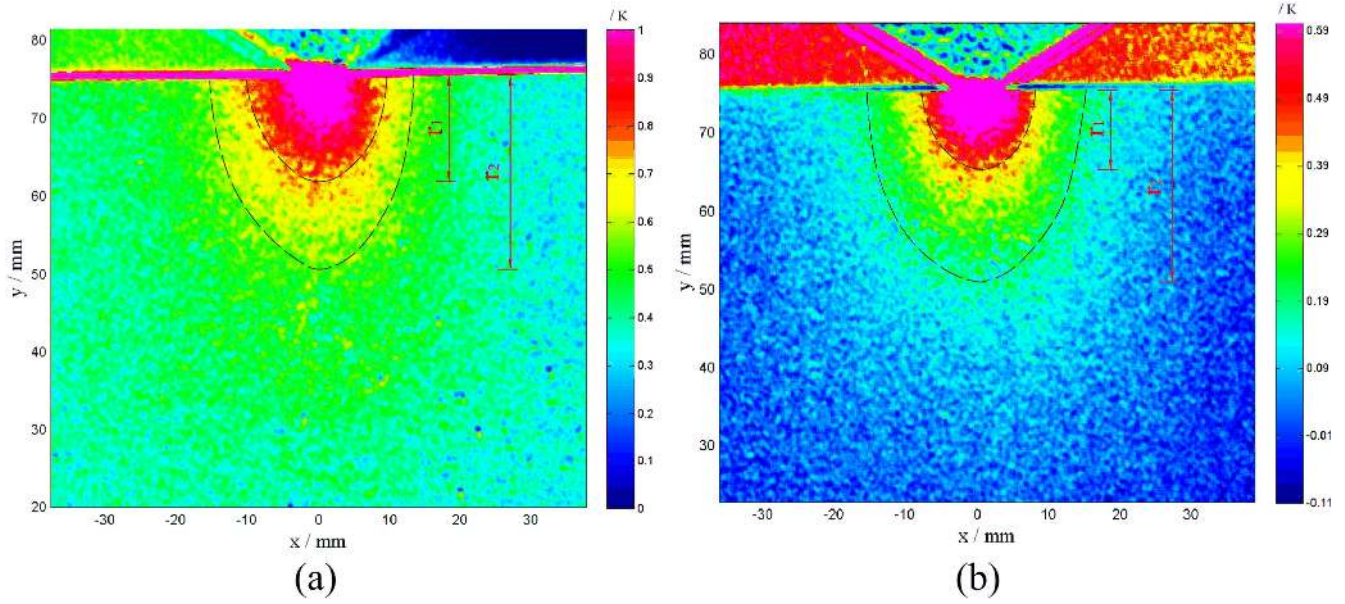$$\frac{p}{\sigma_c} = \frac{1}{K_P - 1}\left(\frac{2K_P}{K_P + 1}\xi_*^{(K_p-1)/K_p} - 1\right). \quad (6)$$

Figure 11. Thermograms of rock samples penetrated by indenters with specific wear flat widths; (a) GW6 and (b) SW6.
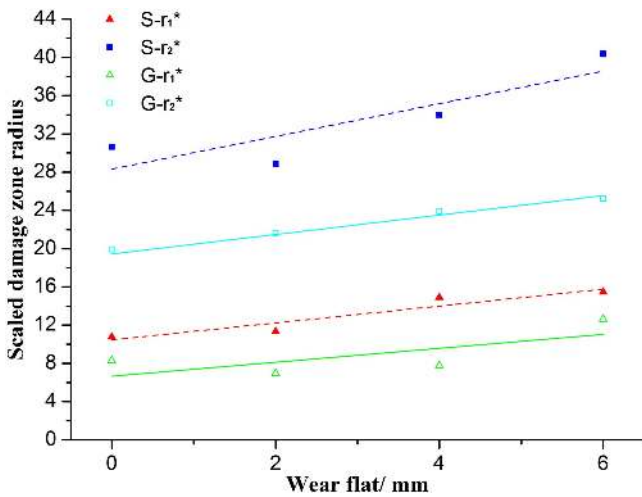

Figure 12. Relationship between the nominal scaled damage zone radii and wear flat widths.
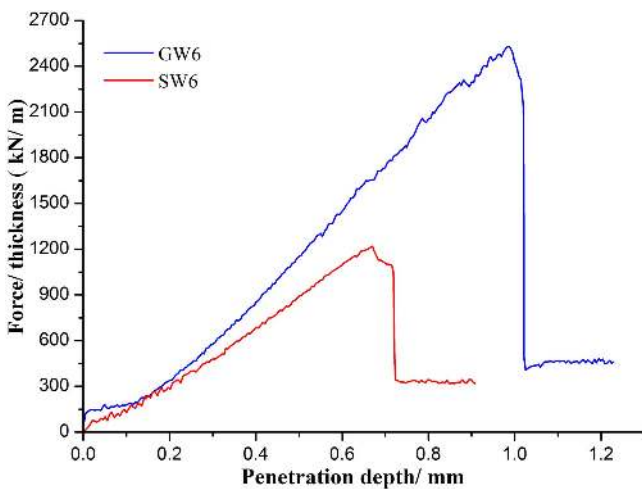

Figure 13. Mechanical responses of granite and sandstone penetrated by the wedge indenter with a wear flat width of 6 mm.
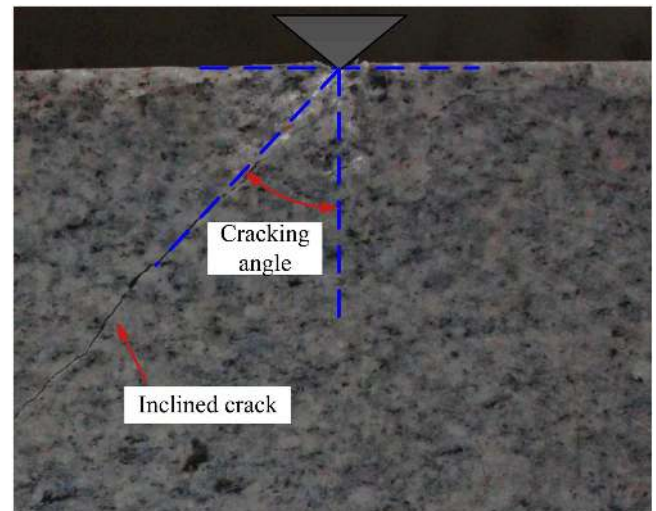

Figure 14. Failure pattern of granite sample GC2.

Wherein, $\xi_*(=r_2/a)$ is the normalized radius of the elasto-plastic interface, a is the indenter-rock contact radius and r_2 is the outer radius of the plastic zone (as shown in figure 5), $p(=F/2a)$ is the indentation pressure, F is the normal force, γ is a constant characterizing the tool geometry and rock properties, K_p and K_d are respectively the passive coefficient and dilatancy coefficient, φ and ψ are respectively the internal friction angle and dilatancy angle of the rock, G $(=E/2(1 + \nu))$ is the shear modulus, β is the included angle between the wedge indenter surface and rock sample.

Table 3 shows the comparison of p and ξ_* between the experimental value and theoretical estimation for granite samples penetrated by indenters with different wedge angles (90°–150°). It is indicated that the CEM based on the Mohr–Coulomb yield criterion underestimates the indentation pressure and overestimates the scaled radius of the elasto-plastic interface. In the classical CEM, it is assumed that the radius of
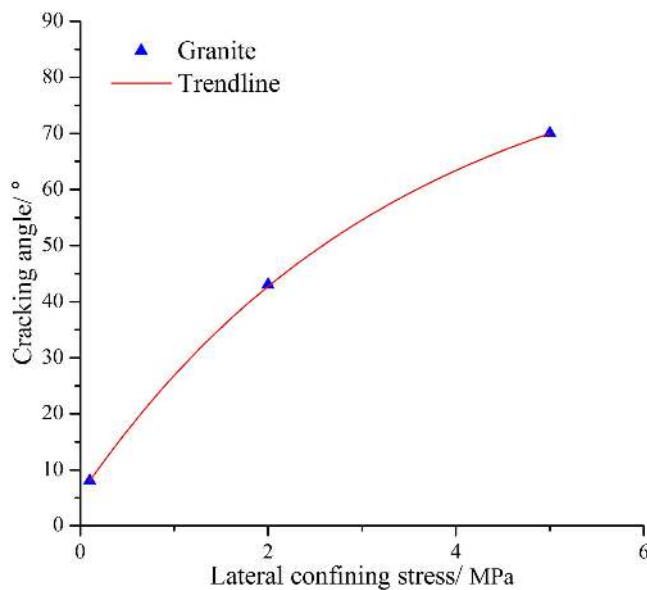
Figure 15. Influence of the lateral confining stress on the cracking angle of rock.

Table 3. The comparison of p and ξ_* between the experimental value and theoretical estimation for granite samples penetrated by indenters with different wedge angles (90°–150°).

Wedge angle		90°	120°	150°
Indentation pressure (p) (MPa)	CEM estimation	449.87	347.73	241.74
	Experimental value	577.64	517.26	248.22
Scaled radius (ξ_*)	CEM estimation	22.94	17.46	11.94
	Experimental value	18.46	11.49	4.67

core zone is equal to the indenter-rock contact radius, but the experimental observation through IRT supports the actual scale of the core zone usually exceeds the semicircle zone. Meanwhile, the simplified hypothesis that the rock behaves as an elastic-perfectly plastic material is also an important theoretical error source. The confirmation of the reason analysis needs the further research.

4.2. Initiation of the critical median crack

For the classical CEM, the linear fracture mechanics has been applied to analyze the macrocrack initiation and propagation, and the critical median crack initiation is thought to occur at the elasto-plastic boundary due to the tensile stress (Huang *et al* 1998, Chen and Labuz 2006, Chen *et al* 2009). However, the experimental observation indicates that there exists a remarkable temperature leap induced by violent microcracking activity near the interface between the core zone and plastic zone just before the cracking point (figure 6(E)). It implies the critical median crack may initiate and propagate from the area in the palstic zone and near the core-plastic interface during the indentation process.

Moreover, before the cracking point, many AE events with high energy cluster in the plastic zone around the core-plastic interface (figure 8(E)), indicating the critical median crack initiation process is accompanied by the violent microcracking activity. It can be also taken as the evidence for above hypothesis about the onset position of the critical median crack. Due to the well-known complexity of contact mechanics and limited application of fracture mechanics around the indenter tip due to the inelastic deformation of rock, it is difficult for the classical analytical solutions to depict the mechanical response of actual fracture occurring there during the indentation process (Lawn and Wilshaw 1975). More precise observations of rock fracturing process under the cutter penetration keep required for further confirmation and analysis, such as application of high-speed photography technique.

5. Conclusions

In the present study, a set of two-dimensional wedge indentation tests on two types of rocks was conducted using nondestructive detection techniques, IRT and AE to experimentally reveal the rock fragmentation mechanism and correlative influence factors of rock indentation. The main results can be summarized as follows:

(1) The phenomenon of discrepant temperature rise on the rock sample surfaces during indentation can be effectively interpreted with the CEM theory. The main mechanisms of the temperature rise in the core zone, plastic zone and elastic zone are attributed to the thermofracture effect, thermoplastic effect and thermoelastic effect, respectively. Different thermomechanical coupling mechanisms can bring about temperature rises with different degrees, and the sizes of different damage zones were quantitatively determined based on the thermal distribution. Observations of the rock damage zone evolution suggest that the plastic zone and core zone initiate and develop sequentially rather than simultaneously.

(2) The wedge indenter with a 120° wedge angle is demonstrated to be more efficient when cutting rock, especially for rock with medium strength like sandstone due to its wider damage zone. When penetrated by wedge indenters with a specific wear flat, the form of rock damage zone is no longer coincident with the semicircular shape of the classical CEM but shows the semiellipse shape. When the wear flat width increases, more indentation work is consumed for the formation of damage zone in the axial direction than that in the transverse direction, which is unfavorable for efficient rock breakage. It is also found that an obvious brittle-ductile transition occurs in the rock failure pattern under indentation when the lateral confining stress exceeds a critical value.

(3) The comparison of the indentation pressure and damage zone size between the experimental value and theoretical estimation indicates there exist some significant differences which may result from the hypotheses of the classical CEM about the core zone scale and mechanical property of rock. Meanwhile, the experimental observation tends to support that the critical median crack initiates and propagates from the area in the plastic zone and near the core-plastic interface during the indentation process, and further experimental and theoretical confirmation keeps required.

Acknowledgments

ORCID iDs

Qi Liu ⓘ https://orcid.org/0000-0002-5658-2471

References

Alehossein H, Detournay E and Huang H 2000 An analytical model for the indentation of rocks by blunt tools *Rock Mech. Rock Eng.* **33** 267–84

ASTM (American Society for Testing and Materials) 2015 *Standard Guide for Determining the Reproducibility of Acoustic Emission Sensor Response* (Philadelphia, USA) Standard E976-15 (https://doi.org/10.1520/E0976-15)

Balci C and Tumac D 2012 Investigation into the effects of different rocks on rock cuttability by a V-type disc cutter *Tunn. Undergr. Space Technol.* **30** 183–93

Bilgin N, Copur H and Balci C 2012 Effect of replacing disc cutters with chisel tools on performance of a TBM in difficult ground conditions *Tunn. Undergr. Space Technol.* **27** 41–51

Brown T E 1981 *Rock Characterization, Testing & Monitoring: ISRM Suggested Methods* (Oxford: Pergamon) pp 219–27

Chen L H, Huang K C and Chen Y C 2009 Acoustic emission at wedge indentation fracture in quasi-brittle *Mater. J. Mech.* **25** 213–23

Chen L H and Labuz J F 2006 Indentation of rock by wedge-shaped tools *Int. J. Rock Mech. Min.* **43** 1023–33

Chiaia B 2001 Fracture mechanisms induced in a brittle material by a hard cutting indenter *Int. J. Solids Struct.* **38** 7747–68

Clienti C, Fargione G, La Rosa G, Risitano A and Risitano G 2010 A first approach to the analysis of fatigue parameters by thermal variations in static tests on plastics *Eng. Fract. Mech.* **77** 2158–67

Cook N G W, Hood M and Tsai F 1984 Observations of crack growth in hard rock loaded by an indenter *Int. J. Rock Mech. Min. Sci. Geomech. Abstr.* **21** 97–107

Dahl F, Grov E and Breivik T 2007 Development of a new direct test method for estimating cutter life, based on the Sievers' J miniature drill test *Tunn. Undergr. Space Technol.* **22** 106–16

Entacher M, Schuller E and Galler R 2015 Rock failure and crack propagation beneath disc cutters *Rock Mech. Rock Eng.* **48** 1559–72

Guclucan Z, Meric S, Palakci Y, Bilgin N, Balci C, Copur H, Namli M, Bilgin A R and Kandemir E 2009 The use of theoretical rock cutting concepts in explaining the cutting performance of a TBM using different cutter types in different rock formations and some recommendations *Proc. World Tunnelling Congress, Safe Tunnelling for the City and for the Environment (Budapest, Hungary)* pp 487–9

Hassanpour J, Rostami J, Tarigh Azali S and Zhao J 2014 Introduction of an empirical TBM cutter wear prediction model for pyroclastic and mafic igneous rocks; a case history of Karaj water conveyance tunnel, Iran *Tunn. Undergr. Space Technol.* **43** 222–31

He M C 2011 Physical modeling of an underground roadway excavation in geologically 45° inclined rock using infrared thermography *Eng. Geol.* **121** 165–76

Huang H, Damjanac B and Detournay E 1998 Normal wedge indentation in rocks with lateral confinement *Rock Mech. Rock Eng.* **31** 81–94

Huang H and Detournay E 2013 Discrete element modeling of tool-rock interaction: II. Rock indentation *Int. J. Numer. Anal. Methods* **37** 1930–47

Innaurato N, Oggeri C, Oreste P P and Vinai R 2007 Experimental and numerical studies on rock breaking with TBM tools under high stress confinement *Rock Mech. Rock Eng.* **40** 429–51

Johnson K L 1970 The correlation of indentation experiments *J. Mech. Phys. Solids* **18** 115–26

La Rosa G, Clienti C and Lo Savio F 2014 Fatigue analysis by acoustic emission and thermographic techniques *Proc. Eng.* **74** 261–8

Lawn B and Wilshaw R 1975 Indentation fracture: principles and applications *J. Mater. Sci.* **10** 1049–81

Lawn B R and Evans A G 1977 A model for crack initiation in elastic/plastic indentation fields *J. Mater. Sci.* **12** 2195–9

Lawn B R and Marshall D B 1984 Indentation fractography: a measure of brittleness *J. Res. Natl Bur. Stand.* **89** 435–51

Li X F, Li H B, Liu Y Q, Zhou Q C and Xia X 2016 Numerical simulation of rock fragmentation mechanisms subject to wedge penetration for TBMs *Tunn. Undergr. Space Technol.* **53** 96–108

Liu H Y, Kou S Q, Lindqvist P A and Tang C A 2002 Numerical simulation of the rock fragmentation process induced by indenters *Int. J. Rock Mech. Min.* **39** 491–505

Ma H S, Yin L J and Ji H G 2011 Numerical study of the effect of confining stress on rock fragmentation by TBM cutters *Int. J. Rock Mech. Min.* **48** 1021–33

Marsh D M 1964 Plastic flow in glass *Proc. R. Soc.* A **279** 420–35

Minh Phono L 1990 Infrared thermovision of damage processes in concrete and rock *Eng. Fract. Mech.* **35** 291–301

Mishnaevsky L L Jr 1995 Physical mechanisms of hard rock fragmentation under mechanical loading: a review *Int. J. Rock Mech. Min. Sci. Geomech. Abstr.* **32** 763–6

Shi W Z, Wu Y H and Wu L X 2007 Quantitative analysis of the projectile impact on rock using infrared thermography *Int. J. Impact Eng.* **34** 990–1002

Song H, Zhang H, Fu D, Kang Y, Huang G, Qu C and Cai Z 2013 Experimental study on damage evolution of rock under uniform and concentrated loading conditions using digital image correlation *Fatigue Fract. Eng. Mater. Struct.* **36** 760–8

Sun N S and Hsu T R 1996 Thermomechanical coupling effects on fractured solids *Int. J. Fract.* **78** 67–87

Sun X M, Xu H C, He M C and Zhang F 2017 Experimental investigation of the occurrence of rockburst in a rock specimen through infrared thermography and acoustic emission *Int. J. Rock Mech. Min.* **93** 250–9

Truman C E, Sackfield A and Hills D A 1995 Contact mechanics of wedge and cone indenters *Int. J. Mech. Sci.* **37** 261–75

Truman C E, Sackfield A and Hills D A 1996 The state of stress induced by a conical indenter *J. Strain Anal. Eng.* **31** 325–7

Wu L X, Cui C Y, Geng N G and Wang J Z 2000 Remote sensing rock mechanics (RSRM) and associated experimental studies *Int. J. Rock Mech. Min.* **37** 879–88

Wu L X, Liu S J, Wu Y H and Wu H P 2002 Changes in infrared radiation with rock deformation *Int. J. Rock Mech. Min.* **39** 825–31

Yadav S, Saldana C and Murthy T G 2015 Deformation field evolution in indentation of a porous brittle solid *Int. J. Solids Struct.* **66** 35–45

Yin L J, Gong Q M, Ma H S, Zhao J and Zhao X B 2014 Use of indentation tests to study the influence of confining stress on rock fragmentation by a TBM cutter *Int. J. Rock Mech. Min.* **72** 261–76

Zhang H, Huang G Y, Song H P and Kang Y L 2012 Experimental investigation of deformation and failure mechanisms in rock under indentation by digital image correlation *Eng. Fract. Mech.* **96** 667–75

Zietlow W K and Labuz J 1998 Measurement of the intrinsic process zone in rock using acoustic emission *Int. J. Rock Mech. Min.* **35** 291–9